Chemical Engineering Journal 379 (2020) 122395

Contents lists available at ScienceDirect

Chemical Engineering Journal

journal homepage: www.elsevier.com/locate/cej

TiO_2/TaS_2 with superior charge separation and adsorptive capacity to the photodegradation of gaseous acetaldehyde

Qinglong Zeng[a,b], Xiao Wang[a], Xiaofeng Xie[a,*], Guanhong Lu[a], Yan Wang[a], Shun Cheng Lee[c], Jing Sun[a]

[a] Shanghai Institute of Ceramics, Chinese Academy of Sciences, Shanghai 200050, China
[b] University of Chinese Academy of Sciences, 19 Yuquan Road, Beijing 100049, China
[c] Department of Civil and Environmental Engineering, Hong Kong Polytechnic University, Hong Kong, China

HIGHLIGHTS

- The introduction of TaS_2 was beneficial for the efficient separation of electron-hole pairs.
- Compared with bare P25, P25/TaS_2 exhibited superior adsorptive capacity.
- $\cdot O_2^-$ played the predominant role while ·OH was the secondary one for the photodegradation of gaseous acetaldehyde.
- This work created the pioneer of the application of TaS_2 in the photocatalytic field.

GRAPHICAL ABSTRACT

Superior charge separation and adsorptive capacity made TiO_2/TaS_2 a good candidate in the photocatalytic field, and $\cdot O_2^-$ was proved to be the main active radical in the photodegradation of gaseous acetaldehyde

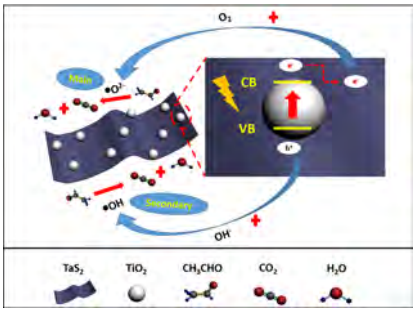

ARTICLE INFO

Keywords:
Photodegradation
TiO_2/TaS_2
2D material
Gaseous acetaldehyde
Superoxide radical

ABSTRACT

Differing from the photocatalysis of liquid contaminant, the capture of gaseous molecule is an essential factor on the photocatalytic activity because of the fast and random motion of gaseous molecule. TaS_2 is a two-dimensional material with good conductivity and large specific area, which are beneficial to the adsorption of gaseous pollutant and the separation of photo-induced e^--h^+ pairs. Here, P25/TaS_2 (P25: commercial TiO_2) was synthesized for the first time to explore the effect of the addition of TaS_2 on the photocatalytic degradation of gaseous acetaldehyde. It turned out that the existence of TaS_2 provided two merits: on the one side, the adsorptive capacity of P25/TaS_2 for gaseous acetaldehyde boosted greatly with the highest adsorptive amount of 234.4 mL, which was three times of that of P25 (76.4 mL); on the other side, the separation efficiency of e^--h^+ pairs of P25/TaS_2 also increased extremely with the highest photo-current response of 15.5 μA/cm^2, which was almost four times of that of P25 (4.2 μA/cm^2). These two merits made P25/TaS_2 have superior photocatalytic activity for the degradation of gaseous acetaldehyde with the highest removal ratio of 98%, which was twice of that of P25 (48%). The cyclic experiments verified that P25/TaS_2 could keep excellent cycling stability after 6 cycles usage. In addition, proved by electron spin resonance (ESR) analyses and radicals quenching tests, superoxide radical was the decisive active species for the degradation of gaseous acetaldehyde compared with hydroxyl radical. Briefly, this work not only created the pioneer of the application of TaS_2 in the photocatalytic field but also verified TaS_2 an efficient co-catalyst in gaseous photocatalysis.

* Corresponding author.
E-mail address: xxfshcn@163.com (X. Xie).

https://doi.org/10.1016/j.cej.2019.122395
Received 2 June 2019; Received in revised form 22 July 2019; Accepted 30 July 2019
Available online 31 July 2019
1385-8947/

1. Introduction

Photocatalysis has been regarded as an available technique to eliminate the detrimental pollutants like VOCs (volatile organic compounds), NO_x, SO_x, which were released into our atmosphere environment by various human activities. TiO_2 is always the most fascinating photocatalyst due to its non-toxicity, abundance, good chemical stability [1–5]. Some reports verified that high removal ratio of Methyl Orange (MO) and Rhodamine B (RhB) could be achieved when applying TiO_2 as photocatalysts in the liquid photocatalysis [6–8]. Differing from the traditional liquid pollutants like Methyl Orange (MO) and Rhodamine B (RhB), for gaseous photocatalysis, it is a challenge for bare TiO_2 to capture the flexible molecules of gaseous pollutant. Hence, incorporating two-dimensional materials such as graphene, C_3N_4 with TiO_2 has attracted much attention in the application of gaseous photocatalysis [9–14]. It turns out that gaseous formaldehyde and propylene could be effectively mineralized by graphene/TiO_2 and C_3N_4/TiO_2, respectively. Therefore, two-dimensional transitional metal dichalcogenides (TMDs) such as MoS_2 and TaS_2 could also have the potential to boost the activity of TiO_2 in gaseous photocatalysis.

Some reports had identified that the introduction of MoS_2 could improve photocatalytic activity of TiO_2 effectively [15,16]. Compared with MoS_2, TaS_2 had much better conductivity, which was beneficial for the separation of photo-induced e^--h^+ pairs. Taking advantage of the superior conductivity of TaS_2, Wu et al. fabricated the micro-supercapacitor with ultrahigh volumetric capacitance of 508F/cm^3 at 10 mV/s and high energy density of 58.5 Wh/L [17]. Li et al. introduced a high density of atomic-scale pores into electrically conductive TaS_2 nanosheets to achieve excellent hydrogen evolution reaction (HER) activities [18]. These studies about TaS_2 mainly focused on its superconductivity and electrocatalysis. TaS_2 is a typical two-dimensional material with excellent conductivity and large specific surface area [17–19], which are the needed advantages of gaseous photocatalysis. However, so far as we know, there are still no reports focusing on the coupling of TaS_2 and TiO_2 in the photocatalytic field. Therefore, in this paper, P25/TaS_2 was synthesized through electrostatic interaction, and its photocatalytic performance was tested by photodegrading gaseous acetaldehyde. Characterizations showed that the addition of TaS_2 increased not only the separation efficiency of photoinduced electron-hole pairs but also the adsorptive amount of gaseous pollutant. Photocurrent response was used to evaluate the separation efficiency of photoinduced electron-hole pairs, it turned out that P25/TaS_2 had much larger photo-current density in comparison to bare P25. S_{BET} and TPD (Temperature programmed desorption) tests were applied to assess the adsorptive capacity of the photocatalysts, the results revealed that the introduction of TaS_2 could improve the physical and chemical adsorption of the photocatalysts for acetaldehyde simultaneously. As a result, P25/TaS_2 exhibited superior photocatalytic ativity than bare P25, and the results showed that P25/TaS_2 had the optimal removal ratio of 98%, which was much higher than that of P25 (48%). In addition, with the help of scavenger experiments, the role of active radicals was investigated. After the addition of TEMPO (scavenger reagent of hydroxyl radicals), a decrease of photocatalytic activity about 22% was observed. While after the addition of PBQ (scavenger reagent of superoxide radicals), the photocatalytic activity declined about 37%. Through combining scavenger experiments tests with ESR tests together, the results revealed that $\cdot O_2^-$ was the main active radical, while ·OH was the secondary one. This work turned out that coupling TaS_2 with P25 was an efficient way to improve the photodegradation ratio of gaseous acetaldehyde, which expanded the application of TaS_2 in photocatalysis field.

2. Experimental conditions

2.1. Chemical materials

P25 powder was supplied by Degussa company. n-butyllithium was supplied by Alfa Aesar. 2H-TaS_2 was purchased from Aladdin Industrial Corporation. MoS_2 was purchased from Shanghai Titan Scientific company. TEMPO (2,2,6,6-tetramethyl-1-piperidinyloxy) was obtained from Aladdin Industrial Corporation, and so does PBQ (p-benzoquinone).

2.2. The chemical exfoliation of Li_xTaS_2 and preparation of TaS_2 nanosheets

The 0.1 g 2H-TaS_2 sample was soaked in 20 mL of 1.6 M n-butyllithium in hexane for 3 days. Then the powder was washed by hexane for three times. Finally the powder was dried under evacuated condition, and then Li_xTaS_2 was obtained. Obtained Li_xTaS_2 sample was soaked in 200 mL distilled water and sonicated for 30 min with magnetic stirring. After sonication, exfoliated TaS_2 nanosheets was produced and a transparent dispersion solution was formed. The obtained transparent dispersion containing exfoliated TaS_2 nanosheets was centrifuged and washed by water for three times. Then, TaS_2 nanosheets were obtained, Scheme 1 was the corresponding schematic of the formation procedure of TaS_2 nanosheets.

2.3. The synthesis of P25/TaS_2

Typically speaking, 3.5, 7, and 14 mg TaS_2 was dispersed in 50 mL deionized water (pH = 3) through ultrasonication. 0.35 g P25 was also dispersed in 50 mL deionized water (pH = 3). Then, P25 suspension was dropped into the aforementioned TaS_2 suspension. Powder sample was obtain through centrifugation and drying. The obtained samples were noted as T1P, T2P, T4P, where T stood for TaS_2 and P for P25, while 1, 2, 4 stood for the weight ratio of TaS_2 to P25 were 1, 2, and 4%, respectively.

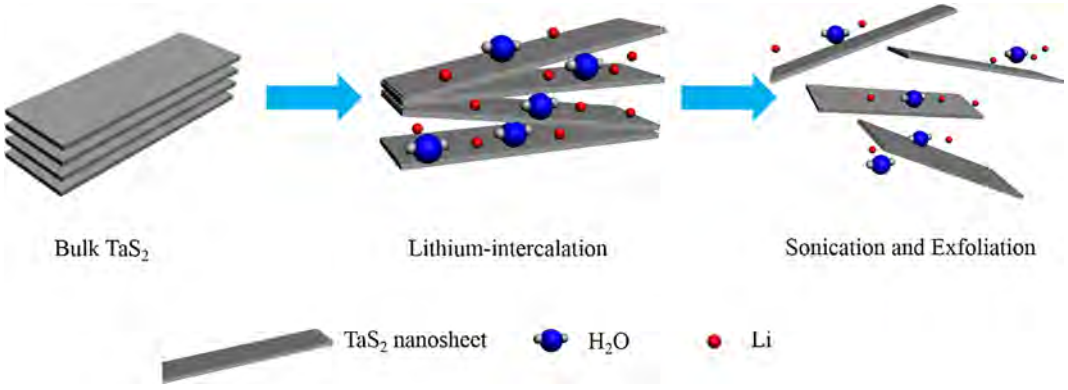

Scheme 1. Schematic of the formation procedure of TaS_2 nanosheet.

2.4. Characterizations

XRD specta were conducted on a X-ray diffractometer (BRUKER AXS GMBH, German). UV–Vis spectra were supplied by a Lambda 950 instrument. Specific surface area (S_{BET}) was collected through a nitrogen adsorption instrument (ASAP 3000). Photoluminescence (PL) measurements were conducted on a Luminescence instrument (LS-55). Magellan 400 (SEM) was used to disclose the surface morphologies of obtain samples. HRTEM images were collected on JEM-2100. Microlab 310F was applied to offer X-ray photoelectron spectroscopy spectra (XPS). TPD (Temperature programmed desorption) measurements were supplied by a gas adsorption apparatus (PCA-1200). Zeta potential measurements were supplied by a zetaPLUS instrument (Brookhaven Instruments). Electron spin resonance measurements (ESR) were supplied by a JES-FA200 instrument. EIS (Electrochemical impedance spectroscopy) measurements were carried out on a three electrode system (CHI 660D), and so do photo-current measurements. AFM measurement was conducted on NT-MDT (NTEGRA, Russia). GC–MS (Gas Chromatography-Mass Spectrometer) analysis was couducted on TSQ 8000 Evo. Scavenger experiments were conducted by applying PBQ and TEMPO to qunch the related $\cdot O_2^-$ and $\cdot OH$.

2.5. Measurement of photocatalytic activity

Gaseous acetaldehyde was selected as targeted pollutant to evaluate the photocatalytic activity. Gas chromatography was used to monitor the concentration of targeted pollutant, the corresponding test system was shown in Scheme 2. Fig. S1 was the related adsorption–desorption curves. The reaction chamber was a cuboid-shaped vessel with the size of 15 cm × 8 cm × 1 cm, and its upper surface was sealed by quartz pane. The catalytic particles were coated onto a glass slide with the size of 12 cm × 5 cm for immobilization. The starting concentration of targeted pollutant was 500 (± 10) ppm, the related flow flux was fixed at 20 sccm, and it was constant which was achieved by flowmeter controller. The removal ratio (X) of targeted pollutant was labeled as $X = (1 - C/C_0) \times 100\%$, in which C_0 was the starting concentration, while C represented the real-time concentration of targeted pollutant (Illuminant: a 260 W fluorescent lamp).

3. Results and discussions

3.1. Characterizations of bulk and exfoliated TaS_2

The phase structure of bulk and exfoliated TaS_2 was disclosed by Raman and XRD analysis. As shown in Fig. 1a (Raman spectra), for exfoliated TaS_2, the relative intensity of the peak located at 287 cm^{-1} decreased a lot, which indicated the exfoliated TaS_2 had thinner thickness compared with bulk TaS_2. Meanwhile, after exfoliation, the peak located at 190 cm^{-1} of bulk TaS_2 shifted to 203 cm^{-1}, this also indicated that the thickness of TaS_2 became thinner during the exfoliated process [20]. Fig. 1b is the XRD spectra of bulk and exfoliated TaS_2, which were both assigned to 2H-TaS_2, and the intensity of the main peak located at $2\theta = 14.6^\circ$ declined a lot after exfoliation. In addition, compared with bulk TaS_2, it was noticed that some XRD diffraction peaks vanished in exfoliated TaS_2. XRD results also indicated that the obtained TaS_2 was in the form of thinner nanosheets [21]. Furthermore, the SEM images of bulk and exfoliated TaS_2 were displayed in Fig. 2a, b, as shown in Fig. 2b, the thickness of exfoliated TaS_2 was about 9.5 nm. Fig. 2c was the AFM image and corresponding height profile, a TaS_2 sheet with a thickness of 6 nm was clearly observed. Namely, the thickness of exfoliated TaS_2 sheets was in nano-scale compared with bulk TaS_2. It was obvious that it is consistent with aforementioned Raman and XRD results.

3.2. Characterizations and surface morphologies of TXP (X = 1,2,4)

As shown in Fig. 3a, the charactristic peaks of anatase and rutile TiO_2 were observed in all samples, because P25 itself was mixed phase structure (70% anatase + 30% rutile). No TaS_2 XRD characteristic peaks were observed in T1P and T2P (Fig. 3a), this could be ascribed to the small content of TaS_2. With the content of TaS_2 increasing to 4%, as shown by the red circle of Fig. 3a, the main peak of TaS_2 located at $2\theta = 14.6^\circ$ was observed in sample T4P. As is well known, the detection sensitivity of XRD tests is approximately 5%, so that TaS_2 could be detected only in T4P. While X-ray photoelectron spectroscopy (XPS) is a more sensitive technique for the detection of chemical element. As shown in Ta4f XPS spectra of P25 (Fig. 4a), there were no Ta4f XPS peaks observed, and it was clearly understandable. While for the Ta4f XPS spectra of T2P, two XPS peaks centered at 24.77 eV and 22.99 eV were observed, which could be ascribed to the XPS characteristic peaks of Ta^{4+} [22]. Similarly, in Fig. 4b, no S element existed in P25, while the XPS characteristic peaks of S^{2-} (161.88 eV and 162.95 eV) were observed in T2P [23]. Briefly, the existence of TaS_2 in T2P was clearly proved.

The interaction between TaS_2 and P25 was investigated by Raman spectra. As shown in Fig. 3b, five Raman peaks (144, 197, 399, 519, and 639 cm^{-1}) were observed, which could be ascribed to characteristic Raman bands of anatase TiO_2 [24], it is in good accordance with aforementioned XRD results. Fig. 3c is the partial enlarged Raman spectra of Fig. 3b, the Raman peak at 144 cm^{-1} of TXP (X = 1, 2, 4) had a blue shift compared with that of P25. It was an indication of residual stress at the contact interface of TaS_2 nanosheets and P25 nanoparticels [25]. This verified the close interaction between TaS_2 nanosheets and P25 nanoparticels. XPS was also a powerful tool to explore the interaction between TaS_2 and P25. As shown in Fig. 4c, there were two peaks in O1s XPS spectra, the one peak (529 eV) was the indication of

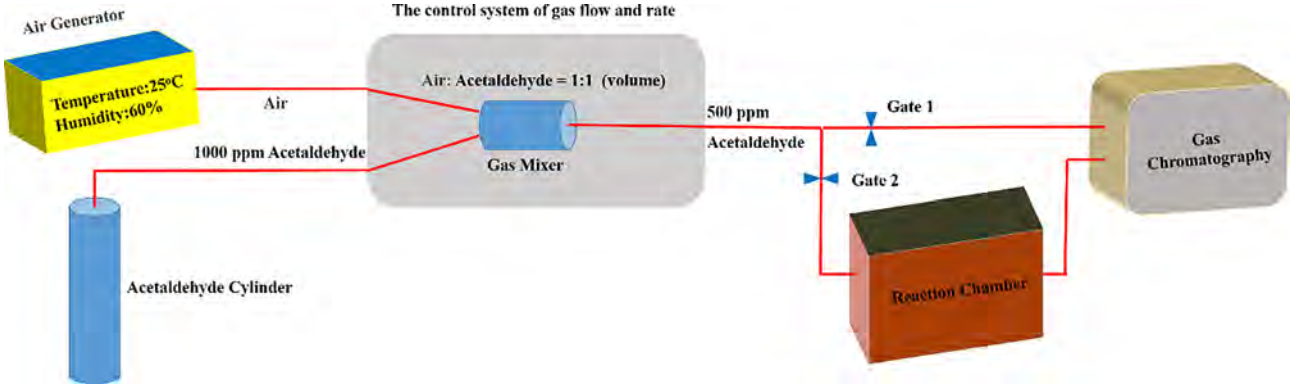

Scheme 2. Schematic of the adsorption and photocatalytic process.

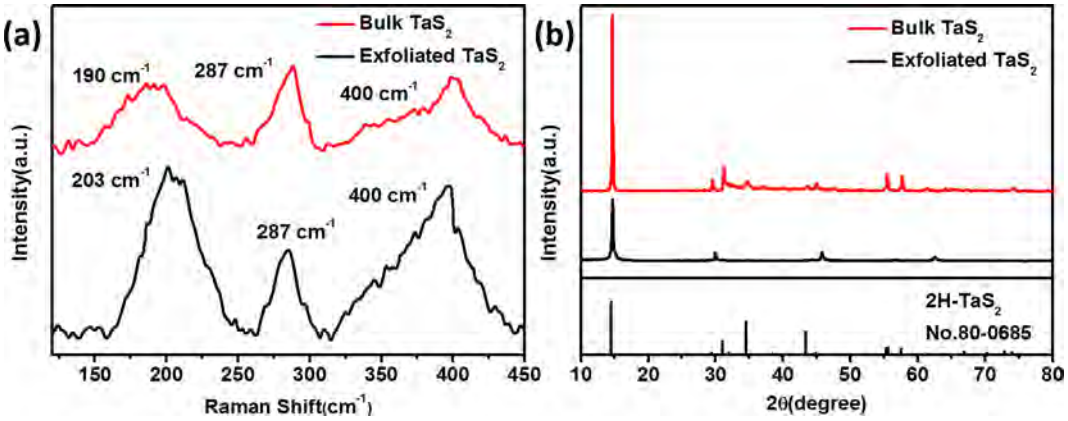

Fig. 1. (a) Raman spectra of bulk TaS_2 and exfoliated TaS_2 (b) XRD spectra of bulk TaS_2 and exfoliated TaS_2.

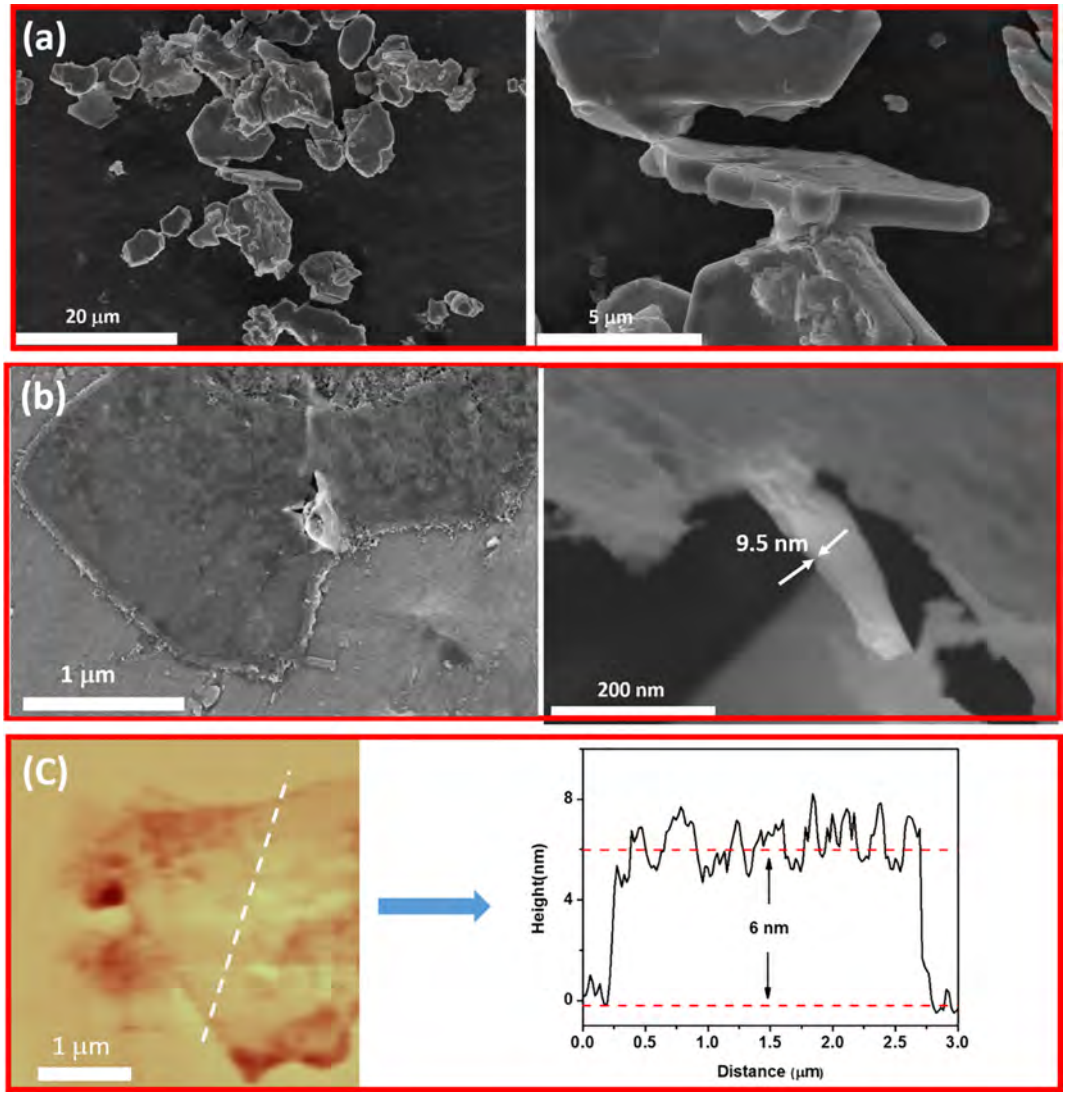

Fig. 2. (a) SEM images of bulk TaS_2 (b) SEM images of exfoliated TaS_2 (c) AFM image and corresponding height profile of exfoliated TaS_2.

Ti-O bond of TiO_2, while the other peak (531 eV) attributed to Ti-OH bond of TiO_2 surface [26]. Besides, compared with P25, there was a 0.1–0.2 eV shift for T2P in O1s XPS spectra. This indicated that the existence of TaS_2 was benefical to the electron transfer of T2P. As for Ti2p XPS spectra of P25 and T2P (Fig. 4d), there were no obvious difference observed. The two Ti2p XPS peaks (458.48 eV, 464.17 eV) were an evidence of the existence of Ti^{4+} [27]. Furthermore, there were characteristic XPS bands of Ti^{3+}or Ti^{2+} observed, which indicated the introduction of TaS_2 had no influence on the valence state of Ti element. As shown in Fig. S2, there were only C, Ti, O XPS peaks observed, which meant there were no other impurities in prepared sample. At the same time, no Ta and S XPS peaks were observed in T2P.

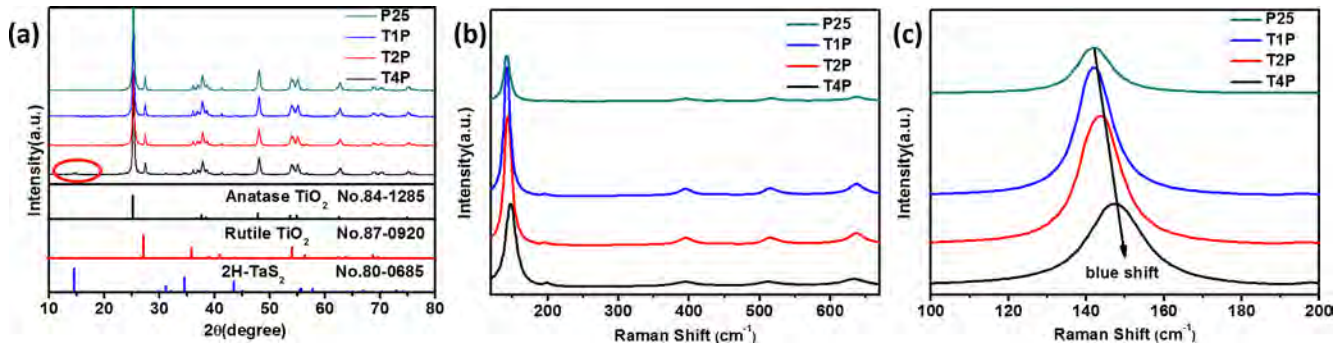

Fig. 3. (a) XRD spectra of P25, T1P, T2P and T4P (b) Raman spectra of P25, T1P, T2P and T4P (c) Enlarged Raman spectra of P25, T1P, T2P and T4P at 144 cm^{-1}.

This could be explained by the low content of TaS_2 and the small amount of TaS_2 was wrapped closely by P25 nanoparticles (Fig. 5). However, high-resolution XPS spectra still verified the existence of Ta and S in T2P (Fig. 4a, b). Similar results could also be obtained from FTIR spectra. As shown in Fig. S3 (FTIR spectra), there were four FTIR bands. The band (3419 cm^{-1}) was beacause of O–H bonds of water. While the peak (1630 cm^{-1}) was due to the bending vibration of water molecules, the bands (581 cm^{-1}, 647 cm^{-1}) were the indication of Ti-O and Ti-O-Ti bonds of TiO_2 lattice [28]. To sum up, the close coupling between TaS_2 nanosheets and P25 nanoparticels was proved by Raman and XPS analysis.

In order to obtain the coupled morphology between TaS_2 nanosheets and P25 nanoparticels, SEM and TEM were used to uncover it. As shown in Fig. S4, the smooth and thin TaS_2 nanosheet was seen clearly, the inset was the corresponding selected area electron diffraction (SAED) image, which was consistent with aforementioned XRD results. As shown in Fig. S5, P25 was made of many nanoparticles with size of 20–30 nm. For the T2P, as revealed by Fig. 5, whatever it is SEM (Fig. 5a, b) or TEM (Fig. 5d, e) images, the coupled morphology that TaS_2 nanosheet was tightly surrounded by many P25 nanoparticels was seen clearly. In addition, corresponding EDS mapping was applied to explore the element distribution, as shown in Fig. 5c, f, four elements (S, Ta, Ti, O) were almost in the same distribution shape. It was a proof of close coupling between TaS_2 and P25. Furthermore, it was easy to find that the P25 nanoparticles dispersed on the TaS_2 nanosheets evenly. The carried charge of TaS_2 and P25 was opposite in the synthesized progress (Fig. S6, PH ≈ 3), so that they could integrate with each other closely. In a word, the close coupling between TaS_2 and P25 in T2P was seen clearly through SEM and TEM.

3.3. The effect of various factors on photocatalysis

It is well-accepted that the light absorption and electron transfer of photocatalyst have great influence on its photocatalytic performance. As shown in Fig. 6a, the light absorption of TXP (X = 1, 2, 4) slightly increased compared with that of P25, which should result from their

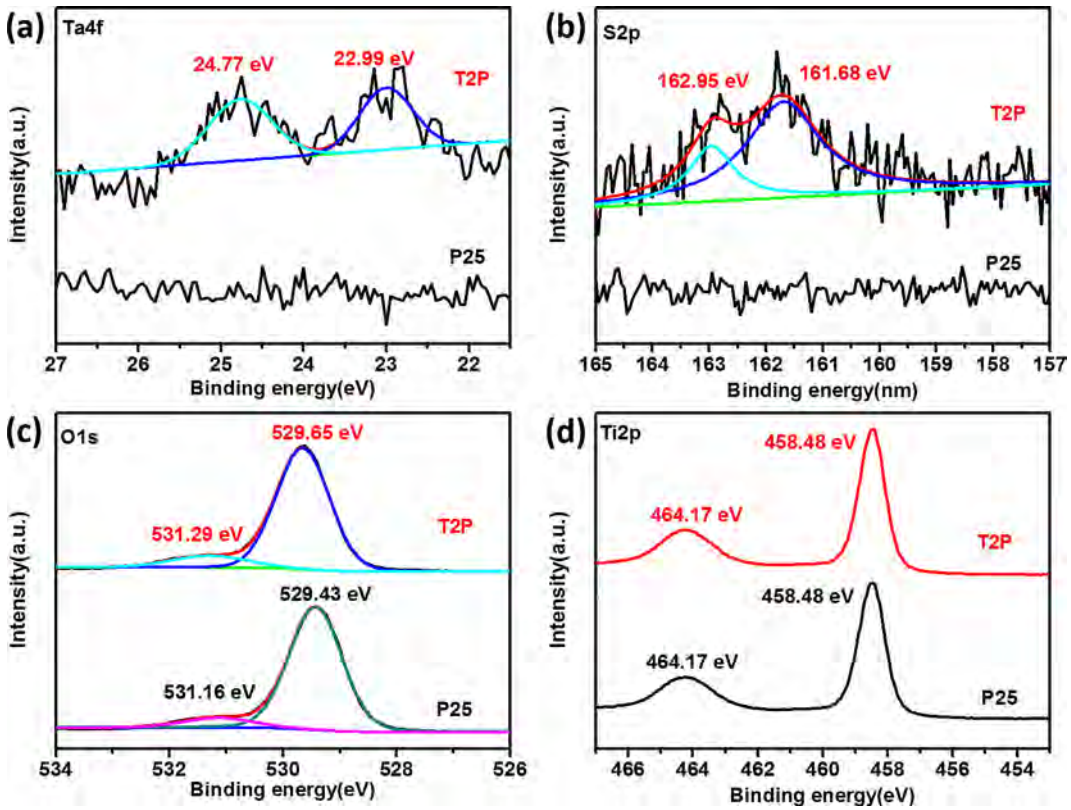

Fig. 4. (a) XPS spectra of Ta4f of P25 and T2P (b) XPS spectra of S2p of P25 and T2P (c) XPS spectra of O1s of P25 and T2P (d) XPS spectra of Ti2p of P25 and T2P.

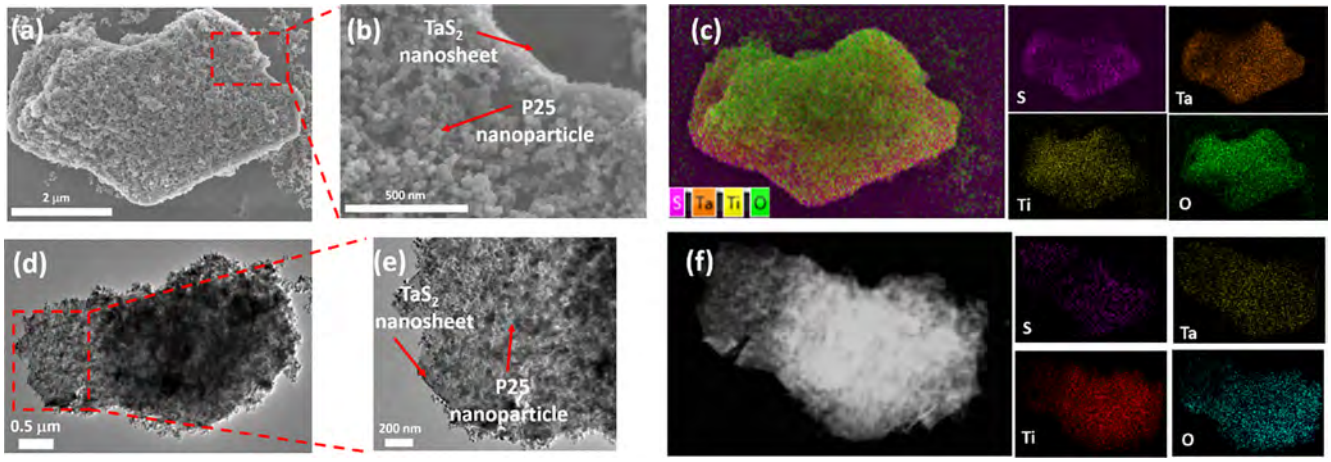

Fig. 5. (a) SEM image of T2P (b) Enlarged SEM image of T2P (c) Corresponding SEM EDS mapping image of T2P (d) TEM image of T2P (e) Enlarged TEM image of T2P (f) Corresponding TEM EDS mapping image of T2P.

slightly darkened appearance. In other words, there was almost no change in the light absorption of these samples. Then, the electron transfer of these samples would play the crucial role on their photocatalytic activity. PL tests is a feasible tool to estimate the activity of electron transfer. As revealed by Fig. 6b, compared with P25, TXP (X = 1, 2, 4) exhibited much weaker PL intensity. Generally speaking, the lower PL intensity usually represented more efficient separation of photo-induced electron-hole pairs [29]. In addition to PL tests, photocurrent response was also an useful technique to monitor the separation of photo-induced electron-hole pairs [30]. As shown in Fig. 7a, TXP (X = 1, 2, 4) exhibited much larger photo-current density in comparison to P25, which was in good agreement with PL results. However, it was easy to find that the PL intensity of T4P did not decrease anymore when the content of TaS_2 was up to 4%. Meanwhile, similarly, the photo-current density of T4P did not increase anymore. Both PL and photo-current tests indicated that excessive TaS_2 loading was harmful to the separation of electron-hole pairs. Excessive TaS_2 would act as recombination center should account for this phenomenon. Studies had proved that excessive Au loading would serve as recombination center [31–33], and the TaS_2 used here was metallic 2H-TaS_2, so excessive TaS_2 could be recombination center. But, in general, the addition of TaS_2 was beneficial for the efficient separation of electron-hole pairs. Electrochemical impedance spectroscopy (EIS) tests also verified this, as shown in Fig. 7b, the transfer resistance of charge could be reflected by the arc size of EIS curves. The smaller arc size generally corresponded to the lower charge transfer resistance [34]. Compared with TXP (X = 1, 2, 4), the biggest EIS arc was observed in P25, which represented the slowest charge separation. In summary, through PL, photo-current and EIS tests, TXP (X = 1, 2, 4) was proved to have the lower charge transfer resistance and faster separation of electron-hole pairs in comparison to bare P25, which were quite significant to improvement of their photocatalytic performance.

For the photocatalysis of gas phase, the adsorptive property of photocatalysts for gaseous pollutant also had a vital effect on their photocatalytic activity. S_{BET} was generally considered as the indicator of the adsorptive property of photocatalysts for gaseous pollutants [35]. The larger the S_{BET} value is, the more gaseous pollutant the photocatalyst could adsorb. Therefore, N_2 adsorption tests was conducted to provide the S_{BET} of these photocatalyst. As shown in Table 1, the measured S_{BET} values were 64, 72, 84, and 103 m^2/g for P25, T1P, T2P, T4P, respectively. TXP (X = 1, 2, 4) had the larger S_{BET} value than P25. In addition, as the amount of TaS_2 increased from 1% to 4%, the corresponding S_{BET} increased from 72 m^2/g to 103 m^2/g. The increased S_{BET} had a positive effect on the photocatalytic performance. However, S_{BET} could only stand for the physical adsorption of photocatalyst. With aim to figure the adsorptive property out, TPD (temperature programmed desorption) tests was conducted to explore the chemical adsorption of the photocatalysts [36,37]. As shown in Fig. 7c, for the adsorption of acetaldehyde, three TPD bands were observed in the spectra, which centered at 200, 450, and 700 °C, respectively. The band of 200 °C was associated with the physical adsorption of photocatalysts, it possessed the lowest intensity among three peaks, which indicated that physical adsorption was the secondary adsorptive form of acetaldehyde. The other two bands located at 450 °C and 700 °C were

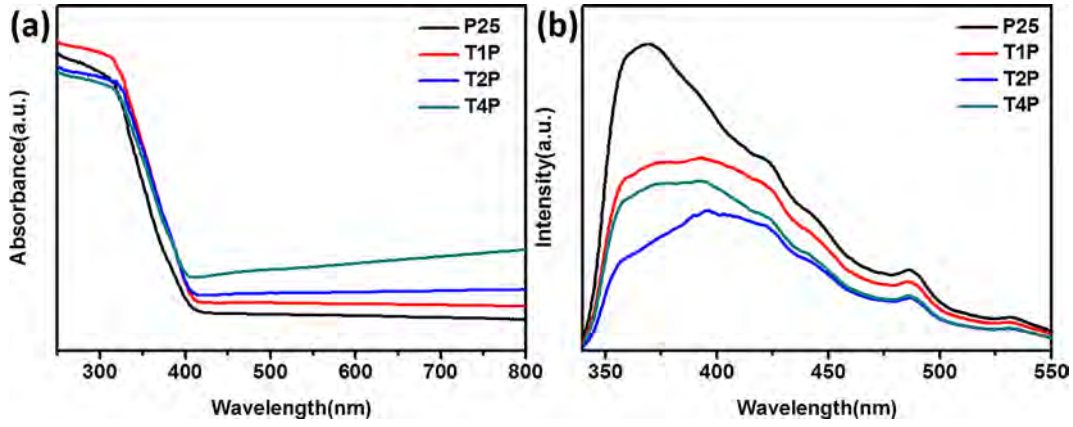

Fig. 6. (a) UV–Vis spectra of P25, T1P, T2P and T4P (b) PL spectra of P25, T1P, T2P and T4P.

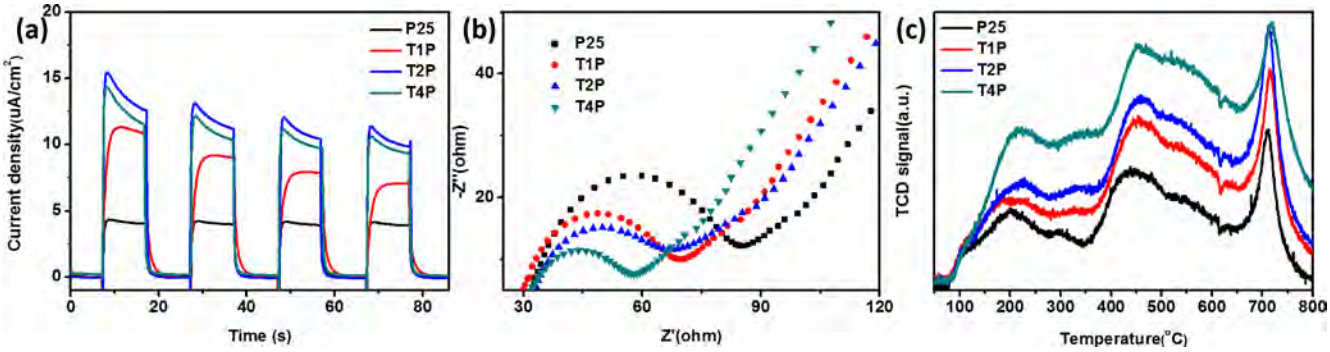

Fig. 7. (a) Photo-current response of P25, T1P, T2P and T4P under AM1.5G irradiation (b) Electrochemical impedance spectroscopy tests of P25, T1P, T2P and T4P (c) TPD tests of P25, T1P, T2P and T4P by using 500 ppm acetaldehyde as the adsorptive gas.

Table 1
S_{BET} area and adsorptive property of P25, T1P, T2P and T4P.

Sample	P25	T1P	T2P	T4P
S_{BET} (m^2/g)	64	72	84	103
Adsorptive amount of acetaldehyde (mL)	76.4	119.6	169.6	234.4

related to the chemical adsorption. Their intensity was higher compared with the band of 200 °C, which indicated that chemical adsorption was the main adsorptive form of acetaldehyde. The higher the TPD intensity is, the stronger the adsorptive capacity is [38,39]. It was easy to find that the TPD intensity of four photocatalysts was in the following order: T4P > T2P > T1P > P25, which was consistent with aforementioned S_{BET} results. Whatever it is physical or chemical adsorption, both S_{BET} and TPD results indicated TXP (X = 1, 2, 4) had more excellent adsorptive capacity for gaseous acetaldehyde than P25. Furthermore, the exact adsorptive amount of targeted pollutant could be calculated through the adsorption-desorption curve by utilizing mathematical integral (Fig. S1). It was already known that the flowing flux of targeted pollutant was about 20 sccm. Then, the adsorptive amount of targeted pollutant could be obtained. The detailed computational process was displayed in Fig. S7. The calculated results were also shown in Table 1, the adsorptive amount of acetaldehyde was 76.4, 119.6, 169.6, and 234.4 mL for P25, T1P, T2P, T4P, respectively. It was worth noted that the S_{BET} of TXP (X = 1, 2, 4) increased only 13% to 64% compared with P25, but with an improved adsorptive capacity of 56% to 301%, which proved the superior physical and chemical adsorption of TaS_2. Briefly, TXP (X = 1, 2, 4) had the superior adsorptive capacity for gaseous acetaldehyde, which was essential to the improvement of their photocatalytic performance.

3.4. The evaluation of photocatalytic performance

The photocatalytic activity of photocatalysts was monitored by the photodegradation of targeted pollutant, which was gaseous acetaldehyde. As shown in Fig. 8a, the removal ratio of acetaldehyde was 48, 92, 98, and 87% for P25, T1P, T2P, T4P, respectively. P25 had the lowest efficiency (48%), all TXP (X = 1, 2, 4) samples had the higher photocatalytic activity than P25, which indicated coupling TaS_2 with P25 could improve the photocatalytic performance efficiently. Besides, as shown in Fig. S8, P25/bulk TaS_2 (2 wt%) had a photocatalytic performance of 55%, which was worse than that of TXP (X = 1, 2, 4) samples (92%, 98% and 87%). The introduction of TaS_2 into P25 mainly brought two advantageous aspects. On the one hand, the existence of TaS_2 elevated the separation efficiency of photoinduced electron–hole pairs (Fig. 6b, Fig. 7a), and also reduced the charge transfer resistance (Fig. 7b). On the other hand, the existence of TaS_2 improved the adsorptive capacity for gaseous acetaldehyde of photocatalysts extremely (Table 1, Fig. 7c, Fig. S7). Among T1P, T2P and T4P, T2P had the highest photocatalytic performance (98%), which was twice as high as P25 (48%). In addition, with the gradually increased content of TaS2 from 1% to 4%, the photocatalytic activity firstly increased from 92% to 98% (T1P to T2P), then declined from 98% to 87% (T2P to T4P). In other words, T2P was the optimal sample. This should be attributed to the synergistic effect of separation efficiency of electron-hole pairs and adsorptive capacity of photocatalysts. When the content of TaS_2 increased from 1% to 2% (T1P to T2P), separation efficiency of electron-hole pairs (Fig. 6b, Fig. 7a) and adsorptive capacity of photocatalysts (Table 1, Fig. 7c, Fig. S7) both increased, then T2P (98%) had the better activity than T1P (92%). However, when the content of TaS_2 increased from 2% to 4% (T2P to T4P), which accompanied with better adsorptive capacity (Table 1, Fig. 7c, Fig. S7) but lower separation efficiency (Fig. 6b, Fig. 7a), then T4P (87%) had

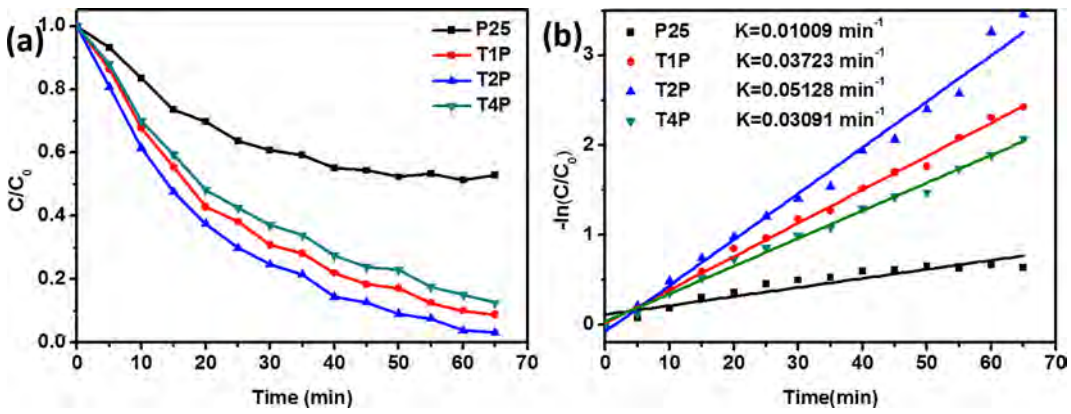

Fig. 8. (a) The photocatalytic performance of P25, T1P, T2P and T4P for gaseous acetaldehyde (b) Kinetic constant calculation of P25, T1P, T2P and T4P.

the worse activity than T2P (98%).Furthermore, the reaction kinetics was explored by the pseudo-first-order kinetic model. The reaction kinetics was calculated through $-\ln(C/C_0) = kt$. As shown in Fig. 8b, the obtained constant k was 0.01009, 0.03723, 0.05128, and 0.03091 min^{-1} for P25, T1P, T2P, T4P, respectively. T2P had the largest reaction kinetics constant k (0.05128 min^{-1}), which was five times larger than that of P25 (0.01009 min^{-1}). It was in agreement with the photocatalytic performance tests (Fig. 8a). In order to know the by-products of photocatalytic process, after the photocatalytic test, the powder sample was collected to do GC–MS (Gas Chromatography-Mass Spectrometer) analysis. As shown in Fig. S9, CH_3CHO and HCOOH were identified, while CH_3CHO was the applied targeted pollutant in our photocatalytic tests. In other words, HCOOH was the main byproduct for the photocatalysis of gaseous acetaldehyde. Furthermore, the photocatalysis of pure MoS_2 and P25/MoS_2 (2 wt%) for gaseous acetaldehyde was measured for comparison (The synthesized process of P25/MoS_2 (2 wt%) was similar to that of TXP). As shown in Fig. S10, pure MoS_2 had no photocatalysis for gaseous acetaldehyde, while P25/MoS_2 (2 wt%) had a 70% removal ratio for gaseous acetaldehyde, which was inferior to that of T2P (98%). This identified that TaS_2 could be a good candidate in the gaseous photocatalytic field.

In addition, two blank tests were carried out to explore whether bare TaS_2 and light would lead to the degradation of targeted pollutant or not. The first one was that bare TaS_2 served as the photocatalyst with other experimental condition unchanged. As shown in Fig. S11, the concentration of gaseous acetaldehyde was not changed at different time, which indicated bare TaS_2 did not have photocatalytic activity at all. Another comparative experiment was conducted with light only but no photocatalysts. As shown in Fig. S12, the concentration of gaseous acetaldehyde was almost identical at different time, which indicated the irradiation light applied in the experiments would not give rise to the decomposition of acetaldehyde. These two comparative experiments verified that bare TaS_2 and light would not lead to the degradation of acetaldehyde.

Taking the practical application into account, the excellent cyclic stability of photocatalysts is indispensable. Therefore, T2P was selected to the representative sample for the cyclic photocatalytic experiments. As shown in Fig. S13, we performed six cyclic experiment on T2P in two weeks. The results indicated that the photocatalyst could remain extremely high photocatalytic performance with no noticeable decrease after sixth circulation, which ensured the photocatalytic stability and efficiency in the long-term practical application.

3.5. The different roles of $\cdot O_2^-$ and ·OH

With aim to figure the roles of $\cdot O_2^-$ and ·OH out, ESR and scavenger experiments analysis were carried out to detect the formation of ·OH and $\cdot O_2^-$. As shown in Fig. 9a, b, all samples exhibited obvious ESR signals, which were the corresponding characteristic peaks of $\cdot O_2^-$ and ·OH [40,41]. The ESR peaks of $\cdot O_2^-$ were observed in Fig. 9a, while Fig. 9b was the ESR signals of ·OH. Whatever it is $\cdot O_2^-$ or ·OH, TXP (X = 1, 2, 4) exhibited stronger ESR signals compared with P25, which indicated TXP (X = 1, 2, 4) could produce more active radicals under the same illumination condition. Then, it is no wonder TXP (X = 1, 2, 4) had superior photocatalysis compared with P25 (Fig. 8a, b). However, it was easy to find that the signals of $\cdot O_2^-$ (Fig. 9a) were stronger than that of ·OH (Fig. 9b) for all samples. It indicated that $\cdot O_2^-$ might play the main role compared with ·OH for the photodegradation of targeted pollutant. Therefore, scavenger experiments were carried out to further verify the role of $\cdot O_2^-$ and ·OH. As shown in Fig. 9c, T2P was selected as the representative photocatalyst to do the corresponding scavenger experiments. $\cdot O_2^-$ (or ·OH) was captured through taking PBQ (or TEMPO) as the related quenching reagent [41,42]. The amount of scavenger reagents used here was enough to quench the related active radicals. As shown in Fig. 9c, when $\cdot O_2^-$ (or ·OH) was captured, the related photocatalytic activity declined a lot, which indicated that both $\cdot O_2^-$ and ·OH played indispensable roles in the photocatalytic process. After the addition of TEMPO (scavenger reagent of hydroxyl radicals), a decrease of photocatalytic activity about 22% was observed (Fig. 9c, red line). While after the addition of PBQ (scavenger reagent of superoxide radicals), the photocatalytic activity declined about 37% (Fig. 9c, blue line). In other words, $\cdot O_2^-$ played a more crucial part compared with ·OH in the photocatalytic process of acetaldehyde. It was in good accordance with aforementioned ESR results (Fig. 9a, b). In summary, through combining scavenger experiments and ESR tests together, it came to a conclusion that both $\cdot O_2^-$ and ·OH played indispensable roles in the photocatalytic process, in which $\cdot O_2^-$ played the dominating part, while ·OH played the secondary one.

Finally, the schematic of efficient photodecomposition of gaseous acetaldehyde by TXP (X = 1, 2, 4) was proposed. As shown in Fig. 10, TiO_2 could produce photoinduced electron-hole pairs under the excitation of illuminant. Then, electron migrated to the CB (conduction band), and leave corresponding hole at VB (valence band). Due to the low transfer resistance of TaS_2, photoinduced electrons would flow from TiO_2 nanoparticles to TaS_2 nanosheets easily, then electron-hole pairs could be separated efficiently. After that, the superoxide radicals were generated by the combination between electrons and oxygen ($O_2 + e^- \rightarrow \cdot O_2^-$). Similarly, the interaction between holes and water resulted in the generation of hydroxyl radicals ($H_2O + h^+ \rightarrow \cdot OH + H^+$). These two active radicals ($\cdot O_2^-$ and ·OH) both possessed strong oxidation capacity, which could mineralize organic pollutant into inorganic molecules. At the same time, the adsorption interaction had been established between acetaldehyde and photocatalyst. Subsequently, it would be decomposed into harmless inorganic molecules (CO_2 and H_2O) by the oxidation of the radicals ($\cdot O_2^-$ and ·OH). Here, for the photodegradation of gaseous acetaldehyde, $\cdot O_2^-$ was the main active radical, while ·OH was the secondary one.

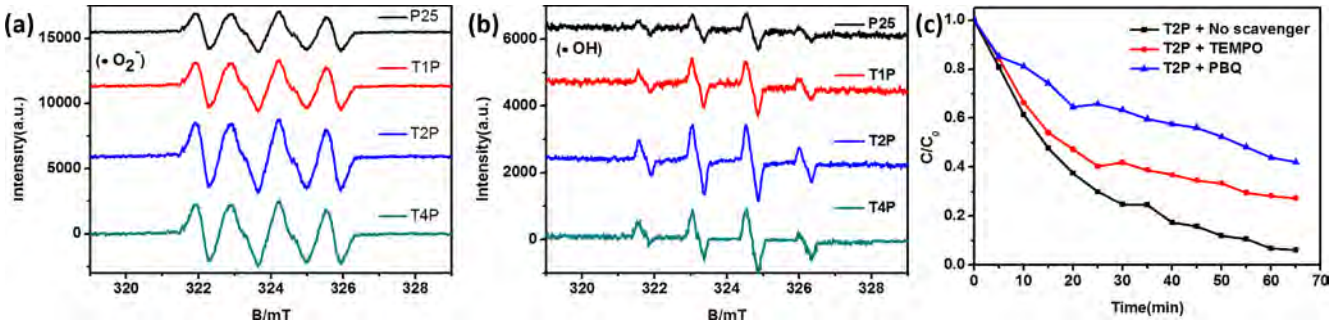

Fig. 9. (a) $\cdot O_2^-$ ESR signals (b) ·OH ESR signals (c) The quenching of $\cdot O_2^-$ and ·OH of T2P by applying related PBQ and TEMPO.

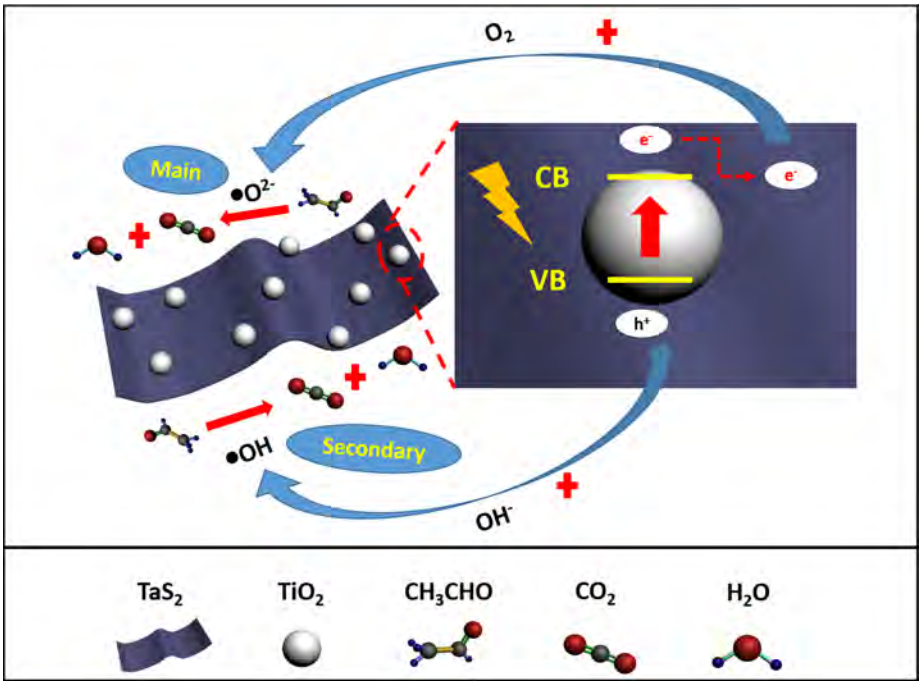

Fig. 10. Schematic of efficient photodecomposition of gaseous acetaldehyde by TXP (X = 1, 2, 4).

4. Conclusions

In summary, TXP (X = 1, 2, 4) was synthesized through the simple electrostatic interaction between TaS_2 nanosheets and P25 nanoparticles. On the one hand, revealed by PL spectra, photo-current response, EIS spectra, with respect to P25, TXP (X = 1, 2, 4) had lower transfer resistance and higher separation efficiency of photoinduced electron-hole pairs. Especially, the photo-current response of the TXP (X = 1, 2, 4) had increased 2–4 times compared with that of P25, which verified the excellent charge separation ability of TaS_2. On the other hand, revealed by TPD tests, S_{BET}, adsorptive capacity, TXP (X = 1, 2, 4) had superior adsorptive capacity of gaseous acetaldehyde than P25. It was worth noted that the S_{BET} of TXP (X = 1, 2, 4) increased only 13% to 64% compared with P25, but with an improved adsorptive capacity of 56% to 301%, which proved the superior physical and chemical adsorption of TaS_2. These two advantages made TXP (X = 1, 2, 4) have better photocatalytic performance than P25. The photocatalytic activity of photocatalysts was estimated through the photodegradation of acetaldehyde, the results showed that T2P had the optimal removal ratio of 98%, which was much higher than that of P25 (48%). In addition, with the aid of ESR and scavenger experiments, the role of active radicals was investigated. It turned out that $\cdot O_2^-$ was the main active radical, while ·OH was the secondary one. This work indicated that incorporating TaS_2 with P25 was an efficient way to boost the photodegradation ratio of gaseous acetaldehyde, which expanded the application of TaS_2 in photocatalysis field.

Declaration of Competing Interest

There are no conflicts to declare.

Acknowledgements

This work was financially supported by the National Key Research and Development Program of China (2016YFA0203000), the NSFC-DFG bilateral organization program (51761135107) and Shanghai Sailing Program (18YF1426800).

Appendix A. Supplementary data

Supplementary data to this article can be found online at https://doi.org/10.1016/j.cej.2019.122395.

References

[1] Z. Wang, C. Yang, T. Lin, H. Yin, P. Chen, D. Wan, F. Xu, F. Huang, J. Lin, X. Xie, M. Jiang, Visible-light photocatalytic, solar thermal and photoelectrochemical properties of aluminium-reduced black titania, Energy Environ. Sci. 6 (2013) 3007.
[2] D.H. Wang, L. Jia, X.L. Wu, L.Q. Lu, A.W. Xu, One-step hydrothermal synthesis of N-doped TiO_2/C nanocomposites with high visible light photocatalytic activity, Nanoscale 4 (2012) 576–584.
[3] B. Qiu, M. Xing, J. Zhang, Mesoporous TiO_2 nanocrystals grown in situ on graphene aerogels for high photocatalysis and lithium-ion batteries, J. Am. Chem. Soc. 136 (2014) 5852–5855.
[4] C.U.I. Xiao-Li, L.I. Hui, L.I. Zhong, M.A. Xiao-Qing, C. Yang, S.U.N. Tong, Facile synthesis of visible light activated carbon-incorporated Mn doped TiO_2 microspheres via flame thermal method, J. Inorg. Mater. 30 (2015) 1002.
[5] H.E. Dan-Nong, Y.A.N. Liang, D. Ya-Mei, T. Qin, High-efficient synthesis and photocatalytic properties of Ag/AgBr/TiO_2 monolithic photocatalysts using sodium alginate as substrate, J. Inorg. Mater. 32 (2017) 637.
[6] N. Riaz, F.K. Chong, B.K. Dutta, Z.B. Man, M.S. Khan, E. Nurlaela, Photodegradation of orange II under visible light using Cu–Ni/TiO_2: Effect of calcination temperature, Chem. Eng. J. 185–186 (2012) 108–119.
[7] B. Cheng, Y. Le, J. Yu, Preparation and enhanced photocatalytic activity of Ag@TiO_2 core-shell nanocomposite nanowires, J. Hazard. Mater. 177 (2010) 971–977.
[8] D. Wu, M. Yi, H. Duan, J. Xu, Q. Wang, Tough TiO_2 -rGO-PDMAA nanocomposite hydrogel via one-pot UV polymerization and reduction for photodegradation of methylene blue, Carbon 108 (2016) 394–403.
[9] M. Zhu, Y. Muhammad, P. Hu, B. Wang, Y. Wu, X. Sun, Z. Tong, Z. Zhao, Enhanced interfacial contact of dopamine bridged melamine-graphene/TiO_2 nano-capsules for efficient photocatalytic degradation of gaseous formaldehyde, Appl. Catal. B 232 (2018) 182–193.
[10] J. Suave, S.M. Amorim, J. Ângelo, L. Andrade, A. Mendes, R.F.P.M. Moreira, TiO_2/reduced graphene oxide composites for photocatalytic degradation in aqueous and gaseous medium, J. Photochem. Photobiol. A 348 (2017) 326–336.
[11] Y. Guo, L. Xiao, M. Zhang, Q. Li, J. Yang, An oxygen-vacancy-rich Z-scheme g-C_3N_4/Pd/TiO_2 heterostructure for enhanced visible light photocatalytic performance, Appl. Surf. Sci. 440 (2018) 432–439.
[12] J.U. Choi, Y.G. Kim, W.-K. Jo, Multiple photocatalytic applications of non-precious Cu-loaded g-C3N4/hydrogenated black TiO_2 nanofiber heterostructure, Appl. Surf. Sci. 473 (2019) 761–769.
[13] W. Lin, X. Xie, X. Wang, Y. Wang, D. Segets, J. Sun, Efficient adsorption and sustainable degradation of gaseous acetaldehyde and o-xylene using rGO-TiO_2 photocatalyst, Chem. Eng. J. 349 (2018) 708–718.
[14] A.Y. Chen, T.T. Zhang, Y.J. Qiu, D. Wang, P. Wang, H.J. Li, Y. Li, J.H. Yang,

X.Y. Wang, X.F. Xie, Construction of nanoporous gold/g-C_3N_4 heterostructure for electrochemical supercapacitor, Electrochim. Acta 294 (2019) 260–267.
[15] C. Wang, H. Lin, Z. Liu, J. Wu, Z. Xu, C. Zhang, Controlled Formation of TiO_2/MoS_2Core-Shell Heterostructures with Enhanced Visible-Light Photocatalytic Activities, Part. Part. Syst. Char. 33 (2016) 221–227.
[16] S. Bai, L. Wang, X. Chen, J. Du, Y. Xiong, Chemically exfoliated metallic MoS_2 nanosheets: A promising supporting co-catalyst for enhancing the photocatalytic performance of TiO_2 nanocrystals, Nano Res. 8 (2014) 175–183.
[17] J. Wu, J. Peng, Z. Yu, Y. Zhou, Y. Guo, Z. Li, Y. Lin, K. Ruan, C. Wu, Y. Xie, Acid-assisted exfoliation toward metallic sub-nanopore TaS_2 monolayer with high volumetric capacitance, J. Am. Chem. Soc. 140 (2018) 493–498.
[18] H. Li, Y. Tan, P. Liu, C. Guo, M. Luo, J. Han, T. Lin, F. Huang, M. Chen, Atomic-sized pores enhanced electrocatalysis of TaS_2 nanosheets for hydrogen evolution, Adv. Mater. 28 (2016) 8945–8949.
[19] E. Navarro-Moratalla, J.O. Island, S. Manas-Valero, E. Pinilla-Cienfuegos, A. Castellanos-Gomez, J. Quereda, G. Rubio-Bollinger, L. Chirolli, J.A. Silva-Guillen, N. Agrait, G.A. Steele, F. Guinea, H.S. van der Zant, E. Coronado, Enhanced superconductivity in atomically thin TaS_2, Nat. Commun. 7 (2016) 11043.
[20] J. Wu, M. Liu, K. Chatterjee, K.P. Hackenberg, J. Shen, X. Zou, Y. Yan, J. Gu, Y. Yang, J. Lou, P.M. Ajayan, Exfoliated 2D transition metal disulfides for enhanced electrocatalysis of oxygen evolution reaction in acidic medium, Adv. Mater. Interfaces 3 (2016) 1500669.
[21] J. Pan, C. Guo, C. Song, X. Lai, H. Li, W. Zhao, H. Zhang, G. Mu, K. Bu, T. Lin, X. Xie, M. Chen, F. Huang, Enhanced superconductivity in restacked TaS_2 nanosheets, J. Am. Chem. Soc. 139 (2017) 4623–4626.
[22] B. Chamlagain, Q. Cui, S. Paudel, M.M.-C. Cheng, P.-Y. Chen, Z. Zhou, Thermally oxidized 2D TaS_2 as a high-κ gate dielectric for MoS_2 field-effect transistors, 2D, Materials 4 (2017) 031002.
[23] W. Xu, T. Wang, Y. Yu, S. Wang, Synthesis of core-shell TiO_2 @MoS_2 composites for lithium-ion battery anodes, J. Alloy. Compd. 689 (2016) 460–467.
[24] Y. Zhu, Q. Ling, Y. Liu, H. Wang, Y. Zhu, Photocatalytic H_2 evolution on MoS_2-TiO_2 catalysts synthesized via mechanochemistry, PCCP 17 (2015) 933–940.
[25] Q. Zeng, X. Xie, X. Wang, Y. Wang, G. Lu, D.Y.H. Pui, J. Sun, Enhanced photocatalytic performance of Ag@TiO_2 for the gaseous acetaldehyde photodegradation under fluorescent lamp, Chem. Eng. J. 341 (2018) 83–92.
[26] H. She, H. Zhou, L. Li, Z. Zhao, M. Jiang, J. Huang, L. Wang, Q. Wang, Construction of a Two-dimensional composite derived from TiO_2 and SnS_2 for enhanced photocatalytic reduction of CO_2 into CH_4, ACS Sustainable Chem. Eng. 7 (2018) 650–659.
[27] Y. Wang, K. Jia, Q. Pan, Y. Xu, Q. Liu, G. Cui, X. Guo, X. Sun, Boron-doped TiO_2 for efficient electrocatalytic N_2 Fixation to NH_3 at ambient conditions, ACS Sustainable Chem. Eng. 7 (2018) 117–122.
[28] H. Dou, D. Long, X. Rao, Y. Zhang, Y. Qin, F. Pan, K. Wu, Photocatalytic degradation kinetics of gaseous formaldehyde flow using TiO_2 nanowires, ACS Sustainable Chem. Eng. 7 (2019) 4456–4465.
[29] H. Li, J. Shang, Z. Ai, L. Zhang, Efficient visible light nitrogen fixation with BiOBr nanosheets of oxygen vacancies on the exposed 001 facets, J. Am. Chem. Soc. 137 (2015) 6393–6399.
[30] G. Li, L. Wu, F. Li, P. Xu, D. Zhang, H. Li, Photoelectrocatalytic degradation of organic pollutants via a CdS quantum dots enhanced TiO_2 nanotube array electrode under visible light irradiation, Nanoscale 5 (2013) 2118–2125.
[31] Y.C. Pu, G. Wang, K.D. Chang, Y. Ling, Y.K. Lin, B.C. Fitzmorris, C.M. Liu, X. Lu, Y. Tong, J.Z. Zhang, Y.J. Hsu, Y. Li, Au nanostructure-decorated TiO_2 nanowires exhibiting photoactivity across entire UV-visible region for photoelectrochemical water splitting, Nano Lett. 13 (2013) 3817–3823.
[32] Y.H. Chiu, K.D. Chang, Y.J. Hsu, Plasmon-mediated charge dynamics and photoactivity enhancement for Au-decorated ZnO nanocrystals, J. Mater. Chem. A 6 (2018) 4286–4296.
[33] J.M. Li, H.Y. Cheng, Y.H. Chiu, Y.J. Hsu, ZnO-Au-SnO_2 Z-scheme photoanodes for remarkable photoelectrochemical water splitting, Nanoscale 8 (2016) 15720–15729.
[34] Y. Xu, C. Zhang, L. Zhang, X. Zhang, H. Yao, J. Shi, Pd-catalyzed instant hydrogenation of TiO_2 with enhanced photocatalytic performance, Energy Environ. Sci. 9 (2016) 2410–2417.
[35] Q. Li, B. Guo, J. Yu, J. Ran, B. Zhang, H. Yan, J.R. Gong, Highly efficient visible-light-driven photocatalytic hydrogen production of CdS-cluster-decorated graphene nanosheets, J. Am. Chem. Soc. 133 (2011) 10878–10884.
[36] M. Chen, J. Ma, B. Zhang, F. Wang, Y. Li, C. Zhang, H. He, Facet-dependent performance of anatase TiO_2 for photocatalytic oxidation of gaseous ammonia, Appl. Catal. B 223 (2018) 209–215.
[37] R.V. Mikhaylov, A.A. Lisachenko, B.N. Shelimov, V.B. Kazansky, G. Martra, S. Coluccia, FTIR and TPD study of the room temperature interaction of a NO–Oxygen mixture and of NO_2 with titanium dioxide, J. Phys. Chem. C 117 (2013) 10345–10352.
[38] J. Luo, K. Kamasamudram, N. Currier, A. Yezerets, NH_3-TPD methodology for quantifying hydrothermal aging of Cu/SSZ-13 SCR catalysts, Chem. Eng. Sci. 190 (2018) 60–67.
[39] J. Wang, F. Han, Y. Rao, T. Hu, Y. Huang, J.-J. Cao, S.C. Lee, Visible-light-driven nitrogen-doped carbon quantum dots/$CaTiO_3$ composite catalyst with enhanced NO adsorption for NO removal, Ind. Eng. Chem. Res. 57 (2018) 10226–10233.
[40] Z. Wang, Y. Huang, W. Ho, J. Cao, Z. Shen, S.C. Lee, Fabrication of $Bi_2O_2CO_3$ /g-C_3N_4 heterojunctions for efficiently photocatalytic NO in air removal: In-situ self-sacrificial synthesis, characterizations and mechanistic study, Appl. Catal. B 199 (2016) 123–133.
[41] X. Ding, W. Ho, J. Shang, L. Zhang, Self doping promoted photocatalytic removal of no under visible light with Bi_2MoO_6: Indispensable role of superoxide ions, Appl. Catal. B 182 (2016) 316–325.
[42] R. Gupta, B. Boruah, J.M. Modak, G. Madras, Kinetic study of Z-scheme C_3N_4/$CuWO_4$ photocatalyst towards solar light inactivation of mixed populated bacteria, J. Photochem. Photobiol., A 372 (2019) 108–121.